Article

Magnetically Collected Platinum/Nickel Alloy Nanoparticles as Catalysts for Hydrogen Evolution

Sebastian Ekeroth, Joakim Ekspong, Dimitrios K. Perivoliotis, Sachin Sharma, Robert Boyd, Nils Brenning, Eduardo Gracia-Espino, Ludvig Edman, Ulf Helmersson,* and Thomas Wagberg*

Read Online

ACCESS | Metrics & More | Article Recommendations | Supporting Information

ABSTRACT: The hydrogen evolution reaction (HER) is a key process in electrochemical water splitting. To lower the cost and environmental impact of this process, it is highly motivated to develop electrocatalysts with low or no content of noble metals. Here, we report on an ingenious synthesis of hybrid Pt_xNi_{1-x} electrocatalysts in the form of a nanoparticle–nanonetwork structure with very low noble metal content. The structure possesses important features such as good electrical conductivity, high surface area, strong interlinking, and substrate adhesion, which render an excellent HER activity. Specifically, the best performing $Pt_{0.05}Ni_{0.95}$ sample demonstrates a Tafel slope of 30 mV dec^{-1} in 0.5 M H_2SO_4 and an overpotential of 20 mV at a current density of 10 mA cm^{-2} with high stability. The impressive catalytic performance is further rationalized in a theoretical study, which provides insight into the mechanism on how such small platinum content can allow for close-to-optimal adsorption energies for hydrogen.

KEYWORDS: *electrocatalyst, hydrogen evolution reaction, pulsed plasma, nanoparticles, metal alloy, electrochemistry, density functional theory, platinum, catalysts, nanoparticles, plasma synthesis*
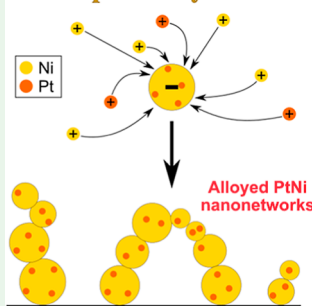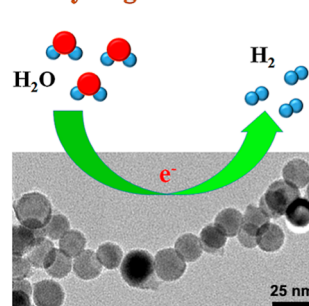
1. INTRODUCTION

Hydrogen can be used, among other things, as a storable energy carrier that can be transformed to electric energy in hydrogen fuel cells. If the hydrogen is produced electrochemically by electrolysis using renewable energy as the driving source, it would represent a sustainable fuel, especially if the two electrochemical half reactions can proceed with low energy losses. The electrocatalysts at the hydrogen evolution cathode and the oxygen evolution anode are the keys to mitigate such undesired energy losses. For the hydrogen evolution reaction (HER) under acidic conditions, Pt has long been regarded as the champion material since it displays optimal adsorption energies for hydrogen.[1,2] Although non-noble metal alternatives, such as various transition metals in combination with sulfides,[3-7] selenides,[8,9] phosphides,[10-12] carbides,[13,14] and nitrides,[15] are reported to exhibit good catalytic activity, they have not been able to outcompete Pt-based catalysts in regard to both efficiency and stability. The common strategies to lower the requirement on noble metals are to decrease the size of the noble metal nanoparticles,[16-18] thereby increasing the surface/volume ratio, or to alloy the noble metal with transition metals, such as Ni,[19,20] Co,[21,22] or Fe.[23,24] Due to their large differences in electronegativity, it is difficult to obtain stable PtNi alloys with controlled Pt/Ni ratio by wet-chemical co-reduction synthesis.[25] Here, we report on the

synthesis of a new hybrid truss-like material named nanonetwork and its utilization as a HER electrocatalyst. The hybrid material comprises necklace-like interconnected nanoparticles with distinct metal–metal interconnections. This leads to very good electrical connection along the whole chain as well as a high surface area due to the interlinked nanoparticles. The catalyst material is produced in a pulsed plasma where the constituent materials form alloyed nanoparticles, which are then collected magnetically into a nanonetwork. In an earlier study, we explained how to collect the alloys of two magnetic materials Fe and Ni.[26] Here, we show that magnetic and non-magnetic elements can also be intermixed into homogeneous alloys and that their atomic ratio can be precisely tuned by the pulsed plasma parameters. Through this innovative and versatile process, we synthesize PtNi alloys that show excellent performance as HER electrocatalysts with extremely low overpotential along with high stability, comparable or even better than similar Pt-based catalysts.[27-29]
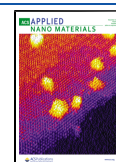
2. EXPERIMENTAL SECTION

2.1. Material Synthesis. The pulsed plasma technique is described in detail in a previous publication.[26] In short, the technique is accomplished by the following procedure. Hollow cathodes of Ni (99.99%) and Pt (99.95%) are placed with their openings close to each other. The cathodes, with a length of 54 mm and an inner diameter of 5 mm, are electrically insulated from each other in order for separate electrical pulses to be delivered to each one. The grounded stainless steel anode ring, 30 mm in diameter, is placed 25 mm from the openings of the cathodes. To confine the plasma, an electrically floating cylindrical stainless steel mesh cage encloses the region defined by the cathode openings and the anode ring. Ar (99.9997%) is used as the process gas and is flown through the two cathodes at a total rate of 120 sccm. A small amount of O_2 is added, from outside the mesh cage, to support nanoparticle nucleation.[30,31] To efficiently add and control the O_2 content, it is diluted in Ar (95%), resulting in an effective flow of 0.025 sccm.

Two HiPSTER 1 pulsing units (Ionautics AB), fed by two MDX-1K dc power supplies (Advanced Energy Industries, Inc.), create pulsed plasmas in each of the cathodes. The reason for using a high-power pulsed technique is to increase the degree of ionization of the sputtered growth material. By using ions, a fast growth of the nanoparticles is achieved, as the positively charged ions are attracted to the nanoparticles, which obtain a negative charge in the plasma.[32,33] The pulse sequence is controlled by a HiPSTER Sync unit. The unit is set to deliver 80 μs long pulses, in sequence to the two cathodes, at a total frequency of 1200 Hz, giving an effective pulsing frequency of 600 Hz to each cathode. This pulse pattern is referred to as *continuous pulsing* in earlier work.[34] The power to the individual cathodes is adjusted, by tweaking the pulse voltage, to tune the amount of sputtered material from each cathode. For most process conditions, the sum of the average power, from the two cathodes, is maintained at 60 W. This is done to avoid overheating of cathodes. However, as the Pt cathode does not provide a stable plasma below 3 W, the total power is raised to 100 W for one experimental condition in order to achieve power ratios below 5% for Pt. In order to compensate for the higher average power, the total deposition time is decreased from 5 to 3 min. All of these parameters are presented in the process conditions table (Supporting Information, Table S1). The substrates are placed on top of a magnet in order to collect the nanoparticles magnetically, as explained in an earlier work.[34−36] However, unlike the previous works, the magnet used here is a permanent cube magnet made from NbFeB with a 7 mm side. This makes the magnetic flux density at the center of the magnet significantly stronger compared to that in the earlier work.[34−36] This results in a more efficient collection of nanoparticles. A schematic illustration of the nanoparticle growth and collection regime is presented in Scheme 1. Si wafers, coated with 200 nm of Ti to yield an electrically conductive surface, are used as substrates for samples used in materials characterization. For the catalysis, depositions are performed onto a carbon paper substrate. The substrates are attached to the magnet using a double-adhesive copper tape. The substrate−magnet assembly is placed on the inside of the mesh at the same lateral distance from the cathode openings as the

anode ring and in a spot of the circumference that gives equidistance to both cathodes.

Samples that are electrically collected are placed on a rotatable substrate holder approximately 20 mm outside an opening in the mesh. The holder, which fits six samples, sits at approximately 150 mm from the cathode openings facing the cathodes through the anode. For details of the geometrical setup, see ref 37.

2.2. Materials Characterization. Grazing incidence X-ray diffraction (GIXRD) experiments are performed using an Empyrean diffractometer in a parallel beam configuration with a line-focused Cu-anode source (Cu Kα_1 = 1.54 nm) operated at 45 kV and 40 mA. The primary beam is adjusted using a parallel beam mirror and a $1/4°$ divergence slit, and in the secondary beam path, a $0.27°$ parallel plate collimator is set. A PIXcel-3D detector is used for data acquisition. The GIXRD scans are performed at an incidence angle of $1°$ in the 2θ range of $30-80°$ using a step size of $0.015°$ and a data acquisition time of 880 ms per step. Scanning electron microscopy (SEM) images were taken using an LEO 1550 instrument with a 5 kV electron beam. All micrographs were taken with a sample tilt of $54°$. To better visualize the complicated structure of the nanonetwork, two images are recorded with different detectors, one located to the side (SE2) and the other from the top (In-lens), to produce a more informative composite image. Scanning transmission electron microscopy (STEM) and transmission electron microscopy (TEM) analyses were performed on selected samples to determine both the internal nanoparticle structure and the interparticle interactions. Prior to STEM and TEM analyses, the nanoparticles were placed onto a copper TEM grid coated with an amorphous layer of carbon. Electrically collected particles were deposited directly onto the grids, while magnetically deposited particles were transferred from the substrate. All measurements were taken using a FEI Tecnai G2 operated at 200 kV. High-angle angular dark-field (HAADF) images were taken with a detector spanning an angular range from 80 to 260 mrad. Energy-dispersive X-ray spectroscopy (EDS) maps were taken with no sample tilting, an acquisition time of 750 ms per spectra, and a resolution of 2 nm. All X-ray photoelectron spectroscopy (XPS) data were collected on an Axis Ultra DLD instrument from Kratos Analytical employing monochromatic Al Kα radiation ($h\nu$ = 1486.6 eV). The spectra were collected from a 0.3×0.7 mm^2 area and with electrons emitted along the surface normal. XPS compositional analysis gave a Pt/Ni ratio of 0.06 along with the high concentration of oxygen. The core spectra of Ni 2p and Pt 4f were peak-fitted using the peak position provided in refs 38 and 39, respectively.

2.3. Electrochemical Measurements. Electrochemical measurements were performed in H_2SO_4 (15 mL, 0.5 M) with a potentiostat (PGSTAT302N, FRA32M module) connected to a three-electrode setup with Ag/AgCl (CHI111-CH Instruments, 1 M KCl) as the reference electrode, a Pt coil as the counter electrode, and the coated carbon paper (Sigracet GDL 34 AA) as the working electrode. A circle with a geometrical area of 0.2 cm^2 was punched out from the coated carbon paper, which was then connected to the potentiostat with a copper wire and sealed with epoxy resin on a microscopic glass slide with only the front side exposed.[40,41] For linear sweep voltammetry, the scan rate was 5 mV s^{-1}. All potentials were corrected after measurement for the solution resistance, measured to 2.5 Ω by electrochemical impedance spectroscopy, and presented versus the reversible hydrogen electrode (RHE) potential by calibrating against a RHE (Gaskatel, Hydroflex). The stability tests were carried out with chronopotentiometry at a current density of 10 mA cm^{-2} for 5−15 h.

2.4. Computational Details. *Ab initio* calculations of the hydrogen adsorption energies on the catalyst particles were performed using density functional theory with the SIESTA code.[42] The generalized gradient approximation with the revised Perdew, Burke, and Ernzerhof parameterization was used to describe the exchange and correlation functional.[43] The valence electrons were represented using linear combinations of pseudo-atomic numerical orbitals with a double-ζ polarized basis.[44] A mesh cutoff of 250 Ry was used to define the real-space grid. The geometrical optimizations of the metal slabs were carried out using a Monkhorst−Pack k-grid of $3 \times 2 \times 1$ and a variable cell scheme by conjugate gradient minimization until

Scheme 1. Schematic Illustration of the Nanoparticle Growth and Collection Regime
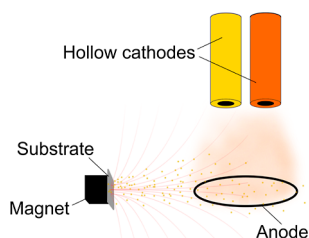
the maximum forces were <0.05 eV Å^{-1}.[45] To calculate the hydrogen adsorption energies on the catalyst particles, (111 and 100) slabs of Ni, Pt, and PtNi alloy models were constructed, where the slabs consist of four atomic layers. A vacuum of 15 Å was added above the structures in the z-direction to avoid interaction between the cells. The Pt atoms were positioned homogenously dispersed in each layer, and the alloy was relaxed together with the cell parameters. For the hydrogen adsorption optimizations, the cell parameters and the two bottom layers of the slabs were kept fixed. The hydrogen adsorption free energies (ΔG_H) were calculated using the computational hydrogen electrode model with a method developed for heterogeneous materials that also calculate and use the equilibrium hydrogen coverages for individual adsorption sites.[46,47] Briefly, this model is separated into two steps where in the first step the hydrogen occupation for each adsorption site is determined by comparing the calculated ΔG_H with a Langmuir adsorption isotherm. In the second step, the final ΔG_H values for each adsorption site are thereafter again calculated using the obtained equilibrium structure and hydrogen coverage from the first step (with a total of 60 geometric optimizations and ΔG_H calculations for 30 adsorption sites). The theoretical voltammetry plots along with exchange current densities were then calculated including all adsorption sites and ΔG_H values following the microkinetic model previously developed for defective and heterogeneous materials.[47] The PtNi-(100) and PtNi-(100) surfaces were evaluated separately and combined without interaction. The adsorption free energy of hydrogen is calculated from the relation $\Delta G_H = \Delta E_H + \Delta E_{ZPE} - T\Delta S$, where ΔE_H is the adsorption energy of hydrogen, ΔE_{ZPE} and ΔS are the difference in zero-point energy and entropy of the adsorbed hydrogen atom and hydrogen in the gas phase. The latter term $\Delta E_{ZPE} - T\Delta S$ has been calculated for similar metals and adsorption sites before and is reused in our calculations.[48] The formation energies of surface slabs were calculated with the relation $E_{form} = E_{total} - N_{Ni}\mu_{Ni} - N_{Pt}\mu_{Pt}$, where E_{total} is the total energy of the metal slabs (PtNi alloy, Ni or Pt) and μ_{Ni} and μ_{Pt} are the chemical potential of Ni and Pt species, respectively, calculated with highly converged fcc unit cells as reference states. N_{Ni} and N_{Pt} are the number of Ni and Pt atoms, respectively, in the structure.

For the simulations of the XRD and the segregated Pt nanoparticles, a spherical nanoparticle with a diameter of 20 nm was constructed directly from the fcc lattice of Ni, the resulting particle had a total of 383913 atoms. Pt doping was carried out in such way that the top four layers (54596 atoms) had an average concentration of 7.3 at. %; however, 50% of the surface had no Pt, so the other half achieved a concentration of ~15 at. %. The remaining Pt atoms were then homogeneously distributed in the rest of the nanoparticle. These conditions are chosen to reflect the experimental conditions, as well as earlier observations on a similar type of alloy nanoparticles.[49] Table S2 shows the Pt distribution in the different nanoparticles following these requirements. The nanoparticles were then geometrically optimized using the large-scale atomic/molecular massively parallel simulator,[50] and the embedded atom potentials for Pt and Ni were from B-Adams *et al.*[51] No periodic boundary conditions were applied, and only conjugate gradient minimization was performed. The as-optimized structure was then used to simulate powder XRD using the Debye scattering formula.[52]

3. RESULTS AND DISCUSSION

To achieve the different elemental compositions of Pt$_x$Ni$_{1-x}$, 0 ≤ x ≤ 1, the power to the two cathodes (Pt and Ni) is regulated separately, yielding different amounts of the sputtered materials in the growth zone of the nanoparticles. The power on the cathodes and other process parameters of the different compositions are given in Table S1, Supporting Information. Figure 1a shows the GIXRD data of the Pt$_x$Ni$_{1-x}$ samples, which were collected either electrically (red curves) or magnetically (black curves). The full range GIXRD data are shown in Figure S1 and Table S3 in the Supporting Information.
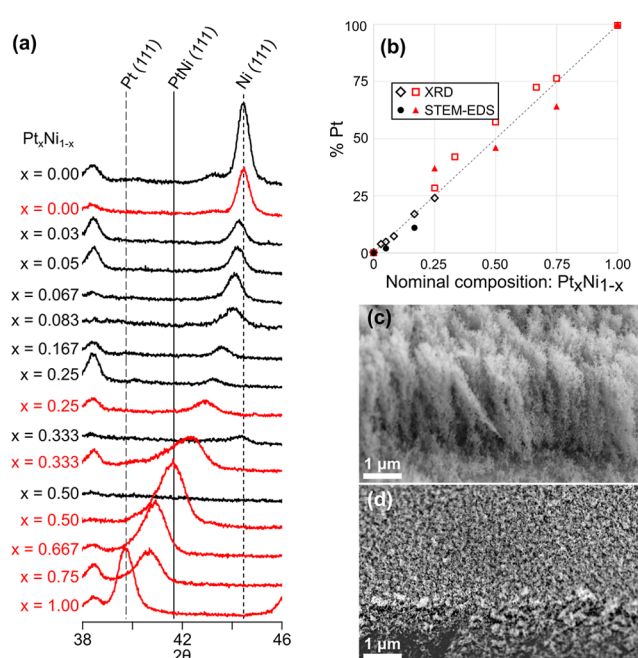

Figure 1. Basic characterization of the Pt$_x$Ni$_{1-x}$ samples. (a) GIXRD of Pt$_x$Ni$_{1-x}$ samples. Magnetically collected nanoparticles are depicted in black, and electrically collected nanoparticles are depicted in red. The nominal Pt$_x$Ni$_{1-x}$ composition is presented to the left of the data. (b) The calculated composition is based on the XRD peak positions in (a) and calculated through Vegard's law and from STEM−EDS measurements. The nominal composition is based on the applied power ratio to the two cathodes. The dashed line is marking the linear 1:1 ratio. SEM side view images of (c) magnetically collected nanoparticles with a composition of Pt$_{0.05}$Ni$_{0.95}$ and (d) electrically collected particles with a composition of Pt$_{0.25}$Ni$_{0.75}$. The number of particles collected electrically is much smaller than that collected magnetically.

The composition factor x used throughout the article relates to the nominal composition given by the power ratio supplied to the two cathodes. A verification that this is a good approximation is seen in Figure 1b, where the nominal composition is plotted against the calculated composition from both XRD and STEM−EDS measurements (see also Figure S2), as described further below.

As shown in an earlier work, the possibility to collect nanoparticles using the magnetic collection technique requires sufficient magnetic properties of the nanoparticles.[35] To determine the limit for magnetic collection of the Pt$_x$Ni$_{1-x}$ nanoparticles, XRD investigations were used. Figure 1a depicts that for magnetically collected samples (black curves), no peaks can be seen for x = 0.50. Moreover, for x = 0.33, we note a small peak corresponding to pure Ni, which is in contrast to samples with lower x that are alloys, as seen in the shift of the Ni(111) peak. As the electrically collected nanoparticles do not form nanonetworks on the substrate, as shown in Figure 1c,d, it is only the magnetic collection that yields nanonetworks desired for the electrocatalytic application. Hence, the composition range for electrocatalytic evaluation is limited to 0 ≤ x ≤ 0.25. However, to illustrate the applicability of the deposition technique, the deposition and growth of the nanoparticles are performed over the full range 0 ≤ x ≤ 1, and for the higher x-values, the nanoparticles had to be electrically collected. The structures shown in Figure 1c were found to be mechanically stable, and previous studies on
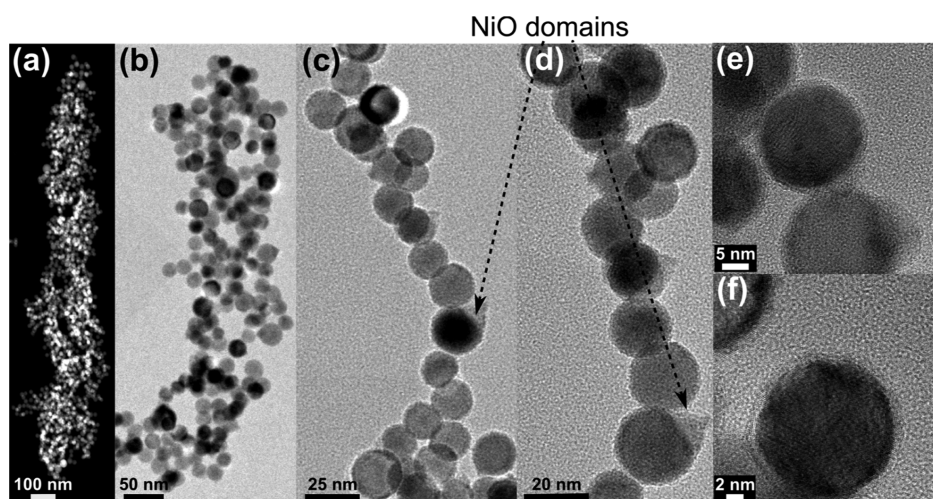
Figure 2. Electron microscopy STEM images highlighting the structure of the $Pt_{0.05}Ni_{0.95}$ nanonetwork. (a) HAADF STEM image showing an individual nanowire. (b−d) Bright-field TEM images showing individual nanoparticles and the bead-on-a-string structure. The triangular features indicated are NiO domains that have grown on the Ni particles. (e,f) HRTEM images of individual particles showing a single crystal core and an oxide shell.
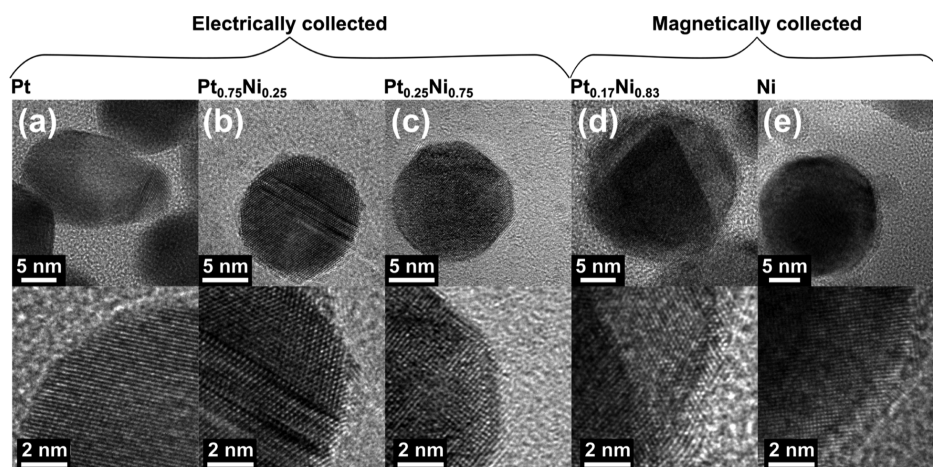

Figure 3. (a−e) HRTEM images of the deposited PtNi nanoparticles. The particles typically consist of one to three different crystal domains. An oxide surface layer is only observed for the Ni-rich particles. For the Ni-rich nanoparticles, there is no apparent separation into Ni-rich and Pt-rich domains.

similar structures based on Fe show, in fact, that the interface between such particles consists of adherent crystalline planes. Furthermore, the nanonetwork structure cannot be easily destroyed; even after treatment with ultrasound, a significant portion of the structures remains intact. This indicates that there is strong and specific adhesion between the individual particles.

The XRD data for all samples (except the magnetically collected x = 0.33 and 0.50) show a dominating peak originating from the (111) planes of the crystal. The position of the (111) plane shifts gradually from Ni(111) to Pt(111) as the nominal composition shifts from pure Ni to pure Pt. In Figure 1b, the peak position and the shift are used in combination with Vegard's law (assuming an ideal solid solution between Pt and Ni) to estimate the alloy composition through the following relation between the lattice parameters (a) of the alloy and the pure elements: $a_{Pt_xNi_{1-x}} = (1 - x)a_{Ni} + xa_{Pt}$.[53] As a complementary method, STEM−EDS was also used to directly analyze individual particles in the case of electrical collection or small fragments of nanochains in the

case of magnetic collection. Both XRD and STEM−EDS prove that the produced particles are Ni/Pt alloys, with the expected compositions, rather than a mixture of separate Ni and Pt particles. It is worth noting that the number of particles analyzed for STEM−EDS is several orders of magnitude lower than that for XRD. For the $Pt_{0.05}Ni_{0.95}$ sample, the measured Pt content by STEM−EDS is significantly lower than expected (2 at. % as opposed to 5 at. %) (Figure S2). This is most likely due to the low signal from the limited amount of Pt and the number of particles analyzed, leading to measurement error. Additional XPS analysis of this sample gave a Pt concentration of 4.7 at. % (Figures S3 and S6). XPS, distinct from the other techniques used here, does not probe the entire particle, rather only the top 5−8 nm.

Figure 2 shows STEM and high-resolution TEM (HRTEM) images of a $Pt_{0.05}Ni_{0.95}$ nanonetwork. The overall structure, Figure 2a, is highly porous, contributing to a high surface-to-volume ratio. Figure 2b−d reveals that the nanoparticles self-organize into interlinked nanowires with a beads-on-a-string architecture. The individual nanoparticles are relatively uni-

form with a size range of 15−25 nm and predominately spherically shaped. The only non-spherical deviation is particles featuring protruding triangular features, which have been identified in the past as NiO domains.[35] The HRTEM images in Figure 2e,f show that the particles consist of a metallic core surrounded by a thin oxide shell. The XPS data in Figure S3a,b provides further support for this conclusion, and after fitting the Ni 2p[38] and Pt 4f peaks,[39] we find that the vast majority of the detectable Ni (97%) is oxidized, whereas 45% of Pt is oxidized.

The presence of an oxide shell can have a strong effect on the properties of the particles, and from the HRTEM images in Figure 3, it appears as if the oxide layers are most pronounced for particles with high Ni content ($Pt_{0.17}Ni_{0.83}$ and pure Ni). The data reveals that the vast majority of the particles consist of a single crystal domain with a small minority consisting of two or three distinct crystal domains, with no apparent separation into different phases.

The electrochemical performance toward the HER of the nanonetwork electrodes was tested and evaluated in 0.5 M H_2SO_4. Figure 4a shows the linear sweep voltammograms for
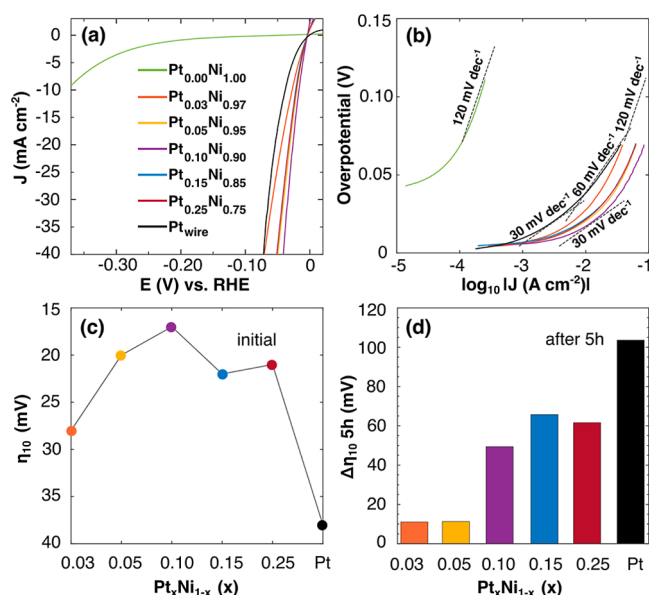

Figure 4. Electrochemical measurements. (a) Measured linear sweep voltammetry in 0.5 M H_2SO_4 for samples with various compositions of Pt_xNi_{1-x} and in the (b) corresponding Tafel plots with Tafel slopes (dashed) of 30, 60, and 120 mV dec^{-1} as guides. (c) Initial overpotential for reaching a current density of 10 mA cm^{-2} and the (d) additional overpotential needed at the same current density but after 5 h tests at 10 mA cm^{-2}.

the Pt_xNi_{1-x} samples with the composition specified in the figure label. In line with expectations, the sample containing no Pt ($x = 0$) shows a very poor activity for HER, albeit with a strong improvement over time, likely due to the reduction of Ni oxides as displayed in the stability study shown in Figure S4a. More noteworthy is that the electrodes already at very low Pt content ($x = 0.03$) reach impressive values for the HER activity and that the $Pt_{0.10}Ni_{0.90}$ electrode initially outcompetes all other sample compositions including the Pt-reference sample, requiring only a potential of 17 mV to reach 10 mA cm^{-2}. This is comparable or better than most other reported data on low noble metal content HER electrocatalysts,[29,54−57] rendering the currently prepared and examined Pt_xNi_{1-x}

materials a promising alternative for further commercial application.

The Tafel plot in Figure 4b shows that all Pt_xNi_{1-x} electrodes feature a Tafel slope of 30 mV dec^{-1} at low current densities, in agreement with the Pt reference electrode, which implies very fast reaction kinetics along with high conductivity and that the chemical recombination desorption of H_2 (Tafel reaction) is the rate-determining reaction step.[47,58] This further shows that the reaction mechanism of the Ni_xPt_{1-x} electrodes resembles that of the pure Pt electrode and that the surface of the Ni_xPt_{1-x} nanoparticles in the nanonetwork electrode probably is rich in Pt atoms, even for the Pt-dilute $Ni_{0.97}Pt_{0.03}$ sample. However, the linear Tafel regions at low current densities are relatively narrow in all Ni_xPt_{1-x} electrodes, which could result from the fact that there are distinct reaction sites with similar activity but with different hydrogen adsorption energies (ΔG_H) and surroundings, which leads to different reaction mechanisms.[47] In particular, two distinctive reaction sites with positive and negative ΔG_H of similar magnitude would result in a combined reaction mechanism with a mixed Tafel slope. A non-linear Tafel slopes at high current densities could also be derived from negative ΔG_H that are optimal ($\Delta G_H \sim 0$ eV).[47] Thus, it is highly likely that the Ni_xPt_{1-x} alloys do not only contain one type of active reaction site as in pure Pt but also have a more complex mechanism. We discuss and test this further below. In all samples, the Tafel slopes increase to 120 mV dec^{-1} at higher current densities, indicating a stabilized hydrogen coverage, which is generally true for any metallic catalysts. Since the linear Tafel regions are relatively narrow, it is difficult to extrapolate exchange current densities (i_0) with high accuracy. Nevertheless, in the low current density region between 5 and 30 mA cm^{-2}, the Tafel slopes are most linear, and the i_0 values of $Ni_{0.90}Pt_{0.10}$ and $Ni_{0.95}Pt_{0.05}$ are then calculated to be −2.6 and −1.8 mA cm^{-2}, respectively.

Figure S4 shows a measurement of the stability of the low-noble metal content Pt_xNi_{1-x} electrodes, as performed by registering the overpotential at 10 mA cm^{-2} for 5 h. The initial overpotentials for reaching 10 mA cm^{-2} of the Pt_xNi_{1-x} alloys are shown in Figure 4c, and in Figure 4d, the additional overpotential needed for reaching the same current density after the stability test is shown. We find that the $Pt_{0.03}Ni_{0.97}$ and $Pt_{0.05}Ni_{0.95}$ electrodes show the best stability, as evidenced by the fact that the required potential has increased by only 11 mV after 5 h. It is also clear that in the H_2SO_4 electrolyte, the stability is better for the low Pt content electrodes and that the higher atomic ratio of Pt leads to faster drop in performance. Such phenomena are not seen in the $HClO_4$ electrolyte, as shown in Figure S4b. This suggests that the Ni-rich electrodes have good ability to cope with the adsorption of sulfur compounds from the electrolyte, which is known to cause problems for Pt surfaces in process gas with high sulfur impurities.[59] The high stability of the nanonetwork electrode is further verified by performing additional long-term durability experiments for our best performing materials, namely, $Pt_{0.05}Ni_{0.95}$ and $Pt_{0.10}Ni_{0.90}$, monitoring the structural and compositional changes by SEM imaging along with EDS and XPS elemental analysis. Interestingly, both $Pt_{0.05}Ni_{0.95}$ and $Pt_{0.10}Ni_{0.90}$ continue to present superior HER activities after 15 h of chronopotentiometric experiment in the H_2SO_4 electrolyte manifested by an increase in the overpotential of 42 and 119 mV at 10 mAcm^{-2}, while the corresponding value for the Pt wire reference is 245 mV (Figure S5). In addition, the SEM
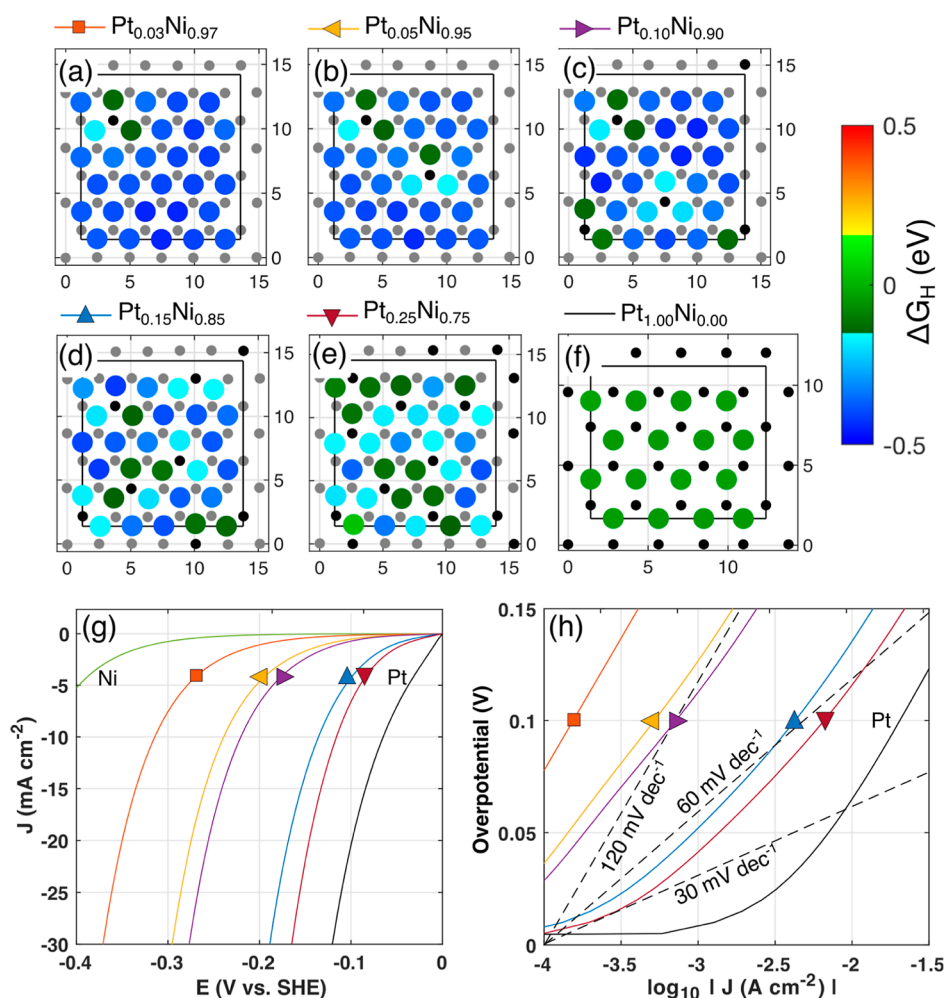
Figure 5. Theoretical results of Pt_xNi_{1-x} systems. (a−f) Catalytic activity maps of $Pt_xNi_{1-x}(111)$ surfaces showing the final coordinates of adsorbed hydrogen for the most energetically stable reaction sites as colored circles with the equilibrium values of ΔG_H according to the color bar. The simulation cells are displayed as black lines and Ni and Pt atoms as gray and black circles, respectively. (g) Theoretical polarization curves for samples with various compositions of Pt_xNi_{1-x}, and in the (h) corresponding Tafel plots with the dashed lines as guides.

images reveal that the nanonetwork architecture remains almost intact after the durability experiment, as shown in Figures S6a,b and S7a,b, further supporting the electrochemical observations. Regarding the compositional changes, the EDS data (Figures S6c and S7c) demonstrate a slight increase in Pt content (3.5 at. %), while this increment is higher (8.0 at. %) when referring to the XPS analysis (Figures S6d and S7d). The latter result indicates that there is a Ni leakage from the particles but that the leakage comes mostly from the outermost PtNi nanoparticle surface. Likely, this creates Pt-rich surfaces that partially explains the high activity of both samples, albeit the low nominal Pt content.

To gain further insights into the high catalytic activity, we performed *ab initio* calculations of Pt_xNi_{1-x} alloys with density functional theory, and the results are shown in Figure 5. To evaluate the alloys, we examined both (111) and (100) surfaces in the fcc lattice. In Figure 5a−f, activity maps of the 111 surfaces are shown, where colored circles indicate the final positions of hydrogen and the equilibrium values of ΔG_H, considering the self-consistency between the DFT-calculated values of ΔG_H and the hydrogen coverage according to the Langmuir adsorption isotherm of the full surface.[47] The results from the (100) surfaces are shown in Figure S8, and plots for the different sites displayed in another fashion are shown in

Figure S9. From Figure 5a, it is clear that for each added Pt atom in the Ni(111) surface, three neighboring adsorption sites are activated, showing more optimal adsorption energies, leading to a high yield in activity gain for each added Pt atom. Theoretical voltammetry plots are further constructed by combining all reaction sites in the Pt_xNi_{1-x} alloys that also comprise a non-interacting mix between 111- and 100-oriented crystal systems with a ratio of 1:1 using a recently developed microkinetic model.[47] From the voltammetry plots in Figure 5f, it is clear that high performances comparable to the experimental samples are only reached for systems with the highest Pt content, that is, $Pt_{0.15}Ni_{0.85}$ and $Pt_{0.25}Ni_{0.75}$. This indicates that all experimental alloys could have a high Pt content in the uppermost surface layer. On the other hand, the theoretical results represent flat surfaces with 1.5×10^{15} reaction sites cm^{-2}, and the high experimental current densities could possibly be due to the high surface area of the 3D structures. Here, we note however that the experimental and theoretical results of pure Ni agree well while having the same structure. Furthermore, the theoretical and experimental Tafel slopes should not be affected by the surface area and can be directly compared. In Figure 5g, we see that the theoretical Tafel plots also do not have any distinct linear regions of 30 mV dec^{-1}, which is caused by various reaction sites and overall

negative values of ΔG_H. The magnitude of the current densities could be more precisely compared if the electrochemical surface area (ECSA) of the experimental samples was known. However, we were not able to determine the ECSA or catalyst loading accurately enough to make a fair comparison.

For theoretical calculations, a common issue for Pt-based materials is that theoretical ΔG_H are slightly negative within the CHE model and Tafel slopes of 30 mV dec^{-1} could thus not be obtained.[47,60] Furthermore, the reaction mechanism on Pt is complex, and it is possible that during electrode polarization, hydrogen adsorbs on less preferable reaction sites for oversaturated surfaces, leading to higher than one monolayer of H-coverage. Such additional hydrogen generally has more positive values of ΔG_H that could result in Tafel slopes of 30 mV dec^{-1}. Yet, the trends and the obtained exchange current densities from our results are still within high accuracy.

Our energetical studies (Figure S10) manifest that the Pt atoms prefer to be close to the surface rather than in the bulk, owing for a rich Pt surface for all Pt_xNi_{1-x} alloys. We also observe that the surfaces are more stable for solid solutions where all Pt atoms are dispersed homogeneously rather than in cluster formation. Together, these two considerations will likely result in solid alloys with slightly Pt-rich surfaces, still avoiding clustering of Pt. Figure S11 shows simulated XRD patterns for $Pt_{0.95}Ni_{0.05}$ with a diameter of 20 nm, where 15% of the Pt atoms have been segregated to the outer four layers, in line with the schematic in Figure S12. The simulated XRD patterns are in very good agreement with Vegard's law and the experimental data (Figure 1a) and support that a Pt-rich skin with fairly high Pt content can be formed at the surface also for nanoparticles with very low Pt concentration (Table S2). The HRTEM images in Figure 5 do not show any separate crystalline domains near the nanoparticle surface for the Ni-rich particles.

4. CONCLUSIONS

To conclude, the nanonetwork Pt_xNi_{1-x} electrocatalyst comprises a homogeneous isotropic metal bulk alloy, with a Pt-enriched surface. The particles demonstrate high conductivity and surface area and are strongly interlinked to each other as well as strongly adhered to the substrate. This leads to an excellent HER activity. The best performing $Pt_{0.05}Ni_{0.95}$ sample demonstrates a Tafel slope of 30 mV dec^{-1} in 0.5 M H_2SO_4 and an overpotential of 20 mV to reach 10 mA cm^{-2}. Theoretical simulations and spectroscopic characterisation further show that the catalytic performance, and the stability in acidic medium, can be explained by a Pt-rich nanoparticle surface. We also showed that each surface Pt atom in the Ni lattice will activate all the neighboring reaction sites, resulting in a high activity relative to Pt content. We believe that our results could be significant not only for electrolysis applications but also for other nearby research fields, such as fuel cells.

■ ASSOCIATED CONTENT

ⓈⒾ Supporting Information

The Supporting Information is available free of charge at https://pubs.acs.org/doi/10.1021/acsanm.1c01676.

Additional experimental details, materials, and calculations (PDF)

■ AUTHOR INFORMATION

Corresponding Authors

Ulf Helmersson − *Department of Physics, Chemistry and Biology, Linköping University, SE-581 83 Linköping, Sweden;* ◎ orcid.org/0000-0002-1744-7322; Email: ulfhe@ifm.liu.se

Thomas Wagberg − *Department of Physics, Umea University, SE-901 87 Umea, Sweden;* ◎ orcid.org/0000-0002-5080-8273; Email: thomas.wagberg@umu.se

Authors

Sebastian Ekeroth − *Department of Physics, Chemistry and Biology, Linköping University, SE-581 83 Linköping, Sweden;* ◎ orcid.org/0000-0002-2264-7345

Joakim Ekspong − *Department of Physics, Umea University, SE-901 87 Umea, Sweden*

Dimitrios K. Perivoliotis − *Department of Physics, Umea University, SE-901 87 Umea, Sweden*

Sachin Sharma − *Department of Physics, Chemistry and Biology, Linköping University, SE-581 83 Linköping, Sweden*

Robert Boyd − *Department of Physics, Chemistry and Biology, Linköping University, SE-581 83 Linköping, Sweden;* ◎ orcid.org/0000-0002-6602-7981

Nils Brenning − *Department of Physics, Chemistry and Biology, Linköping University, SE-581 83 Linköping, Sweden; Division of Space and Plasma Physics, School of Electrical Engineering, KTH Royal Institute of Technology, SE-100 44 Stockholm, Sweden*

Eduardo Gracia-Espino − *Department of Physics, Umea University, SE-901 87 Umea, Sweden;* ◎ orcid.org/0000-0001-9239-0541

Ludvig Edman − *Department of Physics, Umea University, SE-901 87 Umea, Sweden;* ◎ orcid.org/0000-0003-2495-7037

Complete contact information is available at:
https://pubs.acs.org/10.1021/acsanm.1c01676

Notes

The authors declare no competing financial interest.

■ REFERENCES

(1) Strmcnik, D.; Lopes, P. P.; Genorio, B.; Stamenkovic, V. R.; Markovic, N. M. Design principles for hydrogen evolution reaction catalyst materials. *Nano Energy* **2016**, *29*, 29−36.

(2) Conway, B. E.; Tilak, B. V. Interfacial processes involving electrocatalytic evolution and oxidation of H2, and the role of chemisorbed H. *Electrochim. Acta* **2002**, *47*, 3571−3594.

(3) Xie, J.; Zhang, J.; Li, S.; Grote, F.; Zhang, X.; Zhang, H.; Wang, R.; Lei, Y.; Pan, B.; Xie, Y. Controllable disorder engineering in oxygen-incorporated MoS2 ultrathin nanosheets for efficient hydrogen evolution. *J. Am. Chem. Soc.* **2013**, *135*, 17881−17888.

(4) Faber, M. S.; Jin, S. Earth-abundant inorganic electrocatalysts and their nanostructures for energy conversion applications. *Energy Environ. Sci.* **2014**, *7*, 3519−3542.

(5) Ekspong, J.; Sandström, R.; Rajukumar, L. P.; Terrones, M.; Wagberg, T.; Gracia-Espino, E. Stable Sulfur-Intercalated 1T′ MoS2 on Graphitic Nanoribbons as Hydrogen Evolution Electrocatalyst. *Adv. Funct. Mater.* **2018**, *28*, 1802744.

(6) Jaramillo, T. F.; Jørgensen, K. P.; Bonde, J.; Nielsen, J. H.; Horch, S.; Chorkendorff, I. Identification of Active Edge Sites for Electrochemical H2 Evolution from MoS$_2$ Nanocatalysts. *Science* **2007**, *317*, 100.

(7) Li, Y.; Wang, H.; Xie, L.; Liang, Y.; Hong, G.; Dai, H. MoS$_2$ nanoparticles grown on graphene: an advanced catalyst for the hydrogen evolution reaction. *J. Am. Chem. Soc.* **2011**, *133*, 7296–7299.

(8) Gao, M.-R.; Liang, J.-X.; Zheng, Y.-R.; Xu, Y.-F.; Jiang, J.; Gao, Q.; Li, J.; Yu, S.-H. An efficient molybdenum disulfide/cobalt diselenide hybrid catalyst for electrochemical hydrogen generation. *Nat. Commun.* **2015**, *6*, 5982.

(9) Kong, D.; Wang, H.; Lu, Z.; Cui, Y. CoSe$_2$ nanoparticles grown on carbon fiber paper: an efficient and stable electrocatalyst for hydrogen evolution reaction. *J. Am. Chem. Soc.* **2014**, *136*, 4897–4900.

(10) Shi, Y.; Zhang, B. Recent advances in transition metal phosphide nanomaterials: synthesis and applications in hydrogen evolution reaction. *Chem. Soc. Rev.* **2016**, *45*, 1529–1541.

(11) Popczun, E. J.; McKone, J. R.; Read, C. G.; Biacchi, A. J.; Wiltrout, A. M.; Lewis, N. S.; Schaak, R. E. Nanostructured nickel phosphide as an electrocatalyst for the hydrogen evolution reaction. *J. Am. Chem. Soc.* **2013**, *135*, 9267–9270.

(12) Liang, Y.; Liu, Q.; Asiri, A. M.; Sun, X.; Luo, Y. Self-Supported FeP Nanorod Arrays: A Cost-Effective 3D Hydrogen Evolution Cathode with High Catalytic Activity. *ACS Catal.* **2014**, *4*, 4065–4069.

(13) Vrubel, H.; Hu, X. Molybdenum boride and carbide catalyze hydrogen evolution in both acidic and basic solutions. *Angew. Chem., Int. Ed.* **2012**, *51*, 12703–12706.

(14) Zou, X.; Zhang, Y. Noble metal-free hydrogen evolution catalysts for water splitting. *Chem. Soc. Rev.* **2015**, *44*, 5148–5180.

(15) Xie, J.; Li, S.; Zhang, X.; Zhang, J.; Wang, R.; Zhang, H.; Pan, B.; Xie, Y. Atomically-thin molybdenum nitride nanosheets with exposed active surface sites for efficient hydrogen evolution. *Chem. Sci.* **2014**, *5*, 4615–4620.

(16) Han, X.-B.; Tang, X.-Y.; Lin, Y.; Gracia-Espino, E.; Liu, S.-G.; Liang, H.-W.; Hu, G.-Z.; Zhao, X.-J.; Liao, H.-G.; Tan, Y.-Z.; Wagberg, T.; Xie, S.-Y.; Zheng, L.-S. Ultrasmall Abundant Metal-Based Clusters as Oxygen-Evolving Catalysts. *J. Am. Chem. Soc.* **2019**, *141*, 232–239.

(17) Esposito, D. V.; Hunt, S. T.; Stottlemyer, A. L.; Dobson, K. D.; McCandless, B. E.; Birkmire, R. W.; Chen, J. G. Low-Cost Hydrogen-Evolution Catalysts Based on Monolayer Platinum on Tungsten Monocarbide Substrates. *Angew. Chem., Int. Ed.* **2010**, *49*, 9859–9862.

(18) Fang, S.; Zhu, X.; Liu, X.; Gu, J.; Liu, W.; Wang, D.; Zhang, W.; Lin, Y.; Lu, J.; Wei, S.; Li, Y.; Yao, T. Uncovering near-free platinum single-atom dynamics during electrochemical hydrogen evolution reaction. *Nat. Commun.* **2020**, *11*, 1029.

(19) Cao, Z.; Li, H.; Zhan, C.; Zhang, J.; Wang, W.; Xu, B.; Lu, F.; Jiang, Y.; Xie, Z.; Zheng, L. Monocrystalline platinum–nickel branched nanocages with enhanced catalytic performance towards the hydrogen evolution reaction. *Nanoscale* **2018**, *10*, 5072–5077.

(20) Wang, P.; Zhang, X.; Zhang, J.; Wan, S.; Guo, S.; Lu, G.; Yao, J.; Huang, X. Precise tuning in platinum-nickel/nickel sulfide interface nanowires for synergistic hydrogen evolution catalysis. *Nat. Commun.* **2017**, *8*, 14580.

(21) Muntean, R.; Pascal, D.-T.; Rost, U.; Marginean, G.; Brodmann, M.; Vaszilcsin, N. Synthesis and characterisation of platinum–cobalt–manganese ternary alloy catalysts supported on carbon nanofibers: An alternative catalyst for hydrogen evolution reaction. *Int. J. Hydrogen Energy* **2020**, *45*, 26217–26225.

(22) Wang, Z.; Ren, X.; Luo, Y.; Wang, L.; Cui, G.; Xie, F.; Wang, H.; Xie, Y.; Sun, X. An ultrafine platinum–cobalt alloy decorated

cobalt nanowire array with superb activity toward alkaline hydrogen evolution. *Nanoscale* **2018**, *10*, 12302–12307.

(23) Meng, Z.; Xiao, F.; Wei, Z.; Guo, X.; Zhu, Y.; Liu, Y.; Li, G.; Yu, Z.-Q.; Shao, M.; Wong, W.-Y. Direct synthesis of L10-FePt nanoparticles from single-source bimetallic complex and their electrocatalytic applications in oxygen reduction and hydrogen evolution reactions. *Nano Res.* **2019**, *12*, 2954–2959.

(24) Shi, G.; Yano, H.; Tryk, D. A.; Nohara, S.; Uchida, H. High hydrogen evolution activity and suppressed H2O2 production on Pt-skin/PtFe alloy nanocatalysts for proton exchange membrane water electrolysis. *Phys. Chem. Chem. Phys.* **2019**, *21*, 2861–2865.

(25) Yang, H.; Zhang, J.; Kumar, S.; Zhang, H.; Yang, R.; Fang, J.; Zou, S. Monodisperse and highly active PtNi nanoparticles for O$_2$ reduction. *Electrochem. Commun.* **2009**, *11*, 2278–2281.

(26) Ekeroth, S.; Boyd, R.; Brenning, N.; Helmersson, U. Nanowire design by magnetic collection of Fe, Ni and/or FeNi-alloy nanoparticles. **2020**, arXiv:2010.15013.

(27) Li, L.; Wang, S.; Xiong, L.; Wang, B.; Yang, G.; Yang, S. Surface-engineered mesoporous Pt nanodendrites with Ni dopant for highly enhanced catalytic performance in hydrogen evolution reaction. *J. Mater. Chem. A* **2019**, *7*, 12800–12807.

(28) Cheng, N.; Stambula, S.; Wang, D.; Banis, M. N.; Liu, J.; Riese, A.; Xiao, B.; Li, R.; Sham, T.-K.; Liu, L.-M.; Botton, G. A.; Sun, X. Platinum single-atom and cluster catalysis of the hydrogen evolution reaction. *Nat. Commun.* **2016**, *7*, 13638.

(29) Chen, J.; Yang, Y.; Su, J.; Jiang, P.; Xia, G.; Chen, Q. Enhanced Activity for Hydrogen Evolution Reaction over CoFe Catalysts by Alloying with Small Amount of Pt. *ACS Appl. Mater. Interfaces* **2017**, *9*, 3596–3601.

(30) Gunnarsson, R.; Brenning, N.; Boyd, R. D.; Helmersson, U. Nucleation of titanium nanoparticles in an oxygen-starved environment. I: experiments. *J. Phys. D: Appl. Phys.* **2018**, *51*, 455201.

(31) Gunnarsson, R.; Brenning, N.; Ojamäe, L.; Kalered, E.; Raadu, M. A.; Helmersson, U. Nucleation of titanium nanoparticles in an oxygen-starved environment. II: theory. *J. Phys. D: Appl. Phys.* **2018**, *51*, 455202.

(32) Pilch, I.; Söderström, D.; Brenning, N.; Helmersson, U. Size-controlled growth of nanoparticles in a highly ionized pulsed plasma. *Appl. Phys. Lett.* **2013**, *102*, 033108.

(33) Pilch, I.; Söderström, D.; Hasan, M. I.; Helmersson, U.; Brenning, N. Fast growth of nanoparticles in a hollow cathode plasma through orbit motion limited ion collection. *Appl. Phys. Lett.* **2013**, *103*, 193108.

(34) Ekeroth, S. Plasma Synthesis and Self-Assembly of Magnetic Nanoparticles, Doctoral Thesis, Comprehensive Summary; Linkoping University Electronic Press: Linkoping, 2019.

(35) Ekeroth, S.; Ikeda, S.; Boyd, R.; Munger, P.; Shimizu, T.; Helmersson, U. Impact of nanoparticle magnetization on the 3D formation of dual-phase Ni/NiO nanoparticle-based nanotrusses. *J. Nanopart. Res.* **2019**, *21*, 228.

(36) Ekeroth, S.; Munger, E. P.; Boyd, R.; Ekspong, J.; Wagberg, T.; Edman, L.; Brenning, N.; Helmersson, U. Catalytic Nanotruss Structures Realized by Magnetic Self-Assembly in Pulsed Plasma. *Nano Lett.* **2018**, *18*, 3132–3137.

(37) Ekeroth, S.; Ikeda, S.; Boyd, R. D.; Shimizu, T.; Helmersson, U. Growth of semi-coherent Ni and NiO dual-phase nanoparticles using hollow cathode sputtering. *J. Nanopart. Res.* **2019**, *21*, 37.

(38) Liu, F.; Wang, X.; Hao, J.; Han, S.; Lian, J.; Jiang, Q. High Density Arrayed Ni/NiO Core-shell Nanospheres Evenly Distributed on Graphene for Ultrahigh Performance Supercapacitor. *Sci. Rep.* **2017**, *7*, 17709.

(39) Matin, M. A.; Lee, E.; Kim, H.; Yoon, W.-S.; Kwon, Y.-U. Rational syntheses of core–shell Fe@(PtRu) nanoparticle electrocatalysts for the methanol oxidation reaction with complete suppression of CO-poisoning and highly enhanced activity. *J. Mater. Chem. A* **2015**, *3*, 17154–17164.

(40) Sharifi, T.; Gracia-Espino, E.; Jia, X.; Sandström, R.; Wagberg, T. Comprehensive Study of an Earth-Abundant Bifunctional 3D

Electrode for Efficient Water Electrolysis in Alkaline Medium. *ACS Appl. Mater. Interfaces* **2015**, *7*, 28148−28155.

(41) Sharifi, T.; Kwong, W. L.; Berends, H.-M.; Larsen, C.; Messinger, J.; Wagberg, T. Maghemite nanorods anchored on a 3D nitrogen-doped carbon nanotubes substrate as scalable direct electrode for water oxidation. *Int. J. Hydrogen Energy* **2016**, *41*, 69−78.

(42) Soler, J. M.; Artacho, E.; Gale, J. D.; García, A.; Junquera, J.; Ordejón, P.; Sánchez-Portal, D. The SIESTA method forab initioorder-Nmaterials simulation. *J. Phys.: Condens. Matter* **2002**, *14*, 2745−2779.

(43) Hammer, B.; Hansen, L. B.; Nørskov, J. K. Improved adsorption energetics within density-functional theory using revised Perdew-Burke-Ernzerhof functionals. *Phys. Rev. B: Condens. Matter Mater. Phys.* **1999**, *59*, 7413−7421.

(44) Junquera, J.; Paz, O.; Sánchez-Portal, D.; Artacho, E. Numerical atomic orbitals for linear-scaling calculations. *Phys. Rev. B: Condens. Matter Mater. Phys.* **2001**, *64*, 235111.

(45) Monkhorst, H. J.; Pack, J. D. Special points for Brillouin-zone integrations. *Phys. Rev. B: Solid State* **1976**, *13*, 5188−5192.

(46) Nørskov, J. K.; Bligaard, T.; Logadottir, A.; Kitchin, J. R.; Chen, J. G.; Pandelov, S.; Stimming, U. Trends in the Exchange Current for Hydrogen Evolution. *J. Electrochem. Soc.* **2005**, *152*, J23.

(47) Ekspong, J.; Gracia-Espino, E.; Wagberg, T. Hydrogen Evolution Reaction Activity of Heterogeneous Materials: A Theoretical Model. *J. Phys. Chem. C* **2020**, *124*, 20911−20921.

(48) Greeley, J.; Mavrikakis, M. Surface and Subsurface Hydrogen:Adsorption Properties on Transition Metals and Near -SurfaceAlloys. *J. Phys. Chem. B* **2005**, *109*, 3460−3471.

(49) Hu, G.; Nitze, F.; Gracia-Espino, E.; Ma, J.; Barzegar, H. R.; Sharifi, T.; Jia, X.; Shchukarev, A.; Lu, L.; Ma, C.; Yang, G.; Wagberg, T. Small palladium islands embedded in palladium−tungsten bimetallic nanoparticles form catalytic hotspots for oxygen reduction. *Nat. Commun.* **2014**, *5*, 5253.

(50) Plimpton, S. Fast Parallel Algorithms for Short-Range Molecular Dynamics. *J. Comput. Phys.* **1995**, *117*, 1−19.

(51) Adams, J. B.; Foiles, S. M.; Wolfer, W. G. Self-diffusion and impurity diffusion of fcc metals using the five-frequency model and the Embedded Atom Method. *J. Mater. Res.* **2011**, *4*, 102−112.

(52) Farrow, C. L.; Billinge, S. J. L. Relationship between the atomic pair distribution function and small-angle scattering: implications for modeling of nanoparticles. *Acta Crystallogr., Sect. A: Found. Crystallogr.* **2009**, *65*, 232−239.

(53) Denton, A. R.; Ashcroft, N. W. Vegard's law. *Phys. Rev. A* **1991**, *43*, 3161−3164.

(54) Zhang, S. L.; Lu, X. F.; Wu, Z. P.; Luan, D.; Lou, X. W. Engineering Platinum−Cobalt Nano-alloys in Porous Nitrogen-Doped Carbon Nanotubes for Highly Efficient Electrocatalytic Hydrogen Evolution. *Angew. Chem., Int. Ed.* **2021**, *60*, 19068−19073.

(55) Lim, S.-C.; Chan, C.-Y.; Chen, K.-T.; Tuan, H.-Y. Synthesis of popcorn-shaped gallium-platinum (GaPt3) nanoparticles as highly efficient and stable electrocatalysts for hydrogen evolution reaction. *Electrochim. Acta* **2019**, *297*, 288−296.

(56) Fan, A.; Qin, C.; Zhang, X.; Yang, J.; Ge, J.; Wang, S.; Yuan, X.; Wang, S.; Dai, X. Engineering FeNi alloy nanoparticles via synergistic ultralow Pt doping and nanocarbon capsulation for efficient hydrogen evolution. *J. Mater. Chem. A* **2019**, *7*, 24347−24355.

(57) Hu, J.; Fang, C.; Jiang, X.; Zhang, D.; Cui, Z. PtMn/PtCo alloy nanofascicles: robust electrocatalysts for electrocatalytic hydrogen evolution reaction under both acidic and alkaline conditions. *Inorg. Chem. Front.* **2020**, *7*, 4377−4386.

(58) Shinagawa, T.; Garcia-Esparza, A. T.; Takanabe, K. Insight on Tafel slopes from a microkinetic analysis of aqueous electrocatalysis for energy conversion. *Sci. Rep.* **2015**, *5*, 13801.

(59) Tan, S. M.; Sofer, Z.; Pumera, M. Sulfur poisoning of emergent and current electrocatalysts: vulnerability of MoS2, and direct correlation to Pt hydrogen evolution reaction kinetics. *Nanoscale* **2015**, *7*, 8879−8883.

(60) Lindgren, P.; Kastlunger, G.; Peterson, A. A. A Challenge to the G ∼ 0 Interpretation of Hydrogen Evolution. *ACS Catal.* **2019**, *10*, 121−128.